AIAA Science and Technology Forum and Exposition, 3-7 January 2022, San Diego, California

Fluid-Structure Interaction Simulations of the ASPIRE SR01 Supersonic Parachute

Jonathan Boustani[1]*, Francois Cadieux[1]†,
Gaetan K. Kenway[1]‡, Michael F. Barad[1]§, Cetin C. Kiris[1]¶
[1] *Computational Aerosciences Branch, NASA Ames Research Center, Moffett Field, CA 94035, USA.*
Christoph Brehm[2]‖
[2] *Department of Aerospace Engineering, University of Maryland, College Park, MD 20740, USA*

High-fidelity computational fluid dynamics (CFD) simulations have so far only played exploratory and supporting roles in the study and qualification of parachutes for planetary entry. The last few years have seen the maturation of coupled computational methods that are capable of modeling the complex fluid-structure interactions between a parachute canopy and the supersonic flow in the wake of an entry vehicle in flight conditions. One of the primary goals of these methods is to predict the peak opening load experienced by the parachute during inflation. The Launch, Ascent, and Vehicle Aerodynamics (LAVA) team is developing efficient, high-fidelity numerical methods to perform such challenging fluid-structure interaction simulations. A loose coupling approach is used to advance the solutions of a Cartesian ghost cell immersed boundary method CFD solver and a finite element computational structural dynamics (CSD) solver in space and time. The coupled solver is employed to simulate the ASPIRE SR01 flight test, where a build-to-print version of the Mars Science Laboratory parachute was inflated in supersonic conditions in the upper terrestrial atmosphere. The simulations conducted in the current paper predict a peak opening load that is within 10% of that from the flight test. Grid convergence with respect to the volume and structural domains is demonstrated, and less than 1% variation in the peak opening load is predicted between all grid resolutions.

I. Introduction

NASA maintains an excellent track record of landing rovers on the Martian surface using disk-gap-band (DGB) parachutes that deploy at supersonic speeds in the upper atmosphere. Most of these missions benefited from the extensive benchmarking and experimentation that supported the Viking missions.[1] The Mars Science Laboratory (MSL) mission then sought to land the heaviest payload at the highest landing site elevation with the highest level of accuracy yet required. To support this mission, many experiments, wind tunnel tests, and drop tests were conducted, none of which were conducted at supersonic speeds.[2–4] Despite this, the MSL mission was successful in landing the Curiosity rover on the Martian surface.

In an effort to increase the maximum weight that could be delivered to the Martian surface and investigate alternative means of decelerating a supersonic capsule in the Martian atmosphere, NASA and JPL started the low-density supersonic decelerator (LDSD) project.[3] The main concept of these missions was to employ inflatable decelerators followed by large 'disksail' parachutes. Two tests were conducted in 2014 and 2015 in the upper terrestrial atmosphere. In both of these flights, the parachute systems failed either during or shortly after inflation, with large tears forming in the canopy broadcloth. The parachutes were tested in

*Pathways Student, Ph.D. Candidate (University of Kentucky), AIAA member.
†Research Scientist, AIAA member.
‡Research Scientist, AIAA member.
§Senior Research Scientist, AIAA member.
¶Branch Chief, Senior AIAA member.
‖Assistant Professor, AIAA member

subsonic conditions like most tests prior to this, and were designed to withstand loads many times larger than those that induced failure.[5,6]

It became clear that NASA's ability to model and predict stresses during the inflation process was lacking, and a capability to test parachutes in supersonic conditions was developed as part of the Advanced Supersonic Parachute Inflation Research Experiments (ASPIRE) project. The three tests conducted during this project each had DGB parachutes inflate in supersonic conditions in the upper terrestrial atmosphere after being launched via a sounding rocket, one of which is shown in Figs. 1a-c.

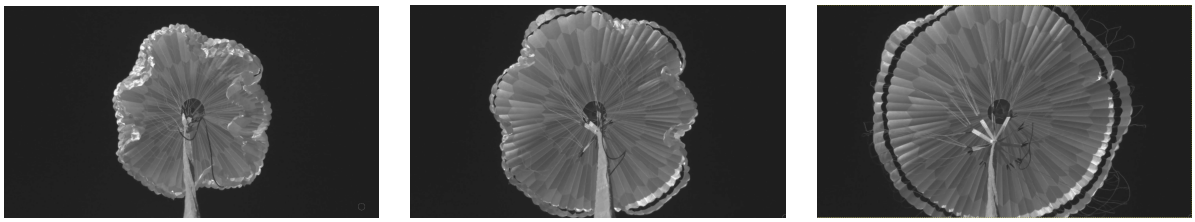


Figure 1: Three snapshots in time of the parachute canopy inflating during the third ASPIRE flight test in the upper terrestrial atmosphere.[7]

Throughout this process, literature shows high-fidelity fluid-structure interaction (FSI) methods playing a primarily supporting role for NASA,[8,9] where most of the simulation efforts were conducted with static and rigid geometries of an inflated parachute canopy.[10–14]

The last few years have seen the maturation of multi-physics (fluid-structural physics) computational methods that are capable of modeling the complex and nonlinear interaction between an inflating parachute canopy and the supersonic flow in the wake of an entry vehicle in representative flight conditions. Works using an Arbitrary-Lagrangian-Eulerian (ALE) formulation include Gao *et al.*,[15] who simulated experiments conducted in support of the MSL parachute.[16] In these experiments, a 0.8 m nominal diameter geometrically-scaled version of the MSL DGB parachute is placed in the wake of a bluff capsule in supersonic conditions. In this work, Gao *et al.*[15] considered a range of Mach numbers and dynamic pressures, and showed the calculated drag values and inflation times to be in good agreement with the experimental values. In 2020, Xue *et al.*,[17] and in 2021, Yang *et al.*,[18] also used an ALE approach with interface tracking to simulate the same experiments and reasonably predict the peak opening loads. Emphasis was placed on the use of 'virtual' structural contact to avoid generating ALE mesh elements with negative volume,[17] and methods for modeling the effect of parachute broadcloth porosity were developed.[18]

Alternative numerical approaches, *e.g.*, immersed boundary methods (IBM), have also been employed to simulate this problem. Large period projected area oscillations in sustained parachute flight were studied by Karagiozis *et al.*[8] using the Favre-filtered Navier-Stokes equations within a Cartesian adaptive mesh refinement framework. This work was recently extended to solving the Favre-filtered compressible Navier-Stokes equations using a PI-controller based IBM.[19] Unfortunately, both works found the presence and strength of parachute area oscillations to depend heavily on the volume grid resolution used. In addition, a recent joint research initiative between the Farhat Research Group at Stanford University and NASA's Jet Propulsion Laboratory[20] is studying the inflation process of supersonic parachutes. This work is based on solving the compressible Navier-Stokes equations using an unstructured, embedded boundary method with adaptive mesh refinement[21] and is considering the effect of the initial folding state and stress state of the canopy on the drag history of a parachute in supersonic flow.

The primary goals of the current work are to demonstrate an alternative capability for simulating supersonic parachute inflation and to systematically study the grid resolution requirements in both the fluid and structural domains. The Launch, Ascent, and Vehicle Aerodynamics (LAVA) team uses efficient, high-fidelity numerical methods to meet these goals. A loose coupling approach is used to advance the solutions of a computational fluid dynamics (CFD) and a computational structural dynamics (CSD) solver in space and time.

The LAVA-Cartesian CFD solver considers the compressible Navier-Stokes equations discretized on a block-structured Cartesian grid with adaptive mesh refinement. Geometries are immersed into the Cartesian grid using a ghost-cell method in order to sharply represent the fluid-structure interface. The LAVA-Structural CSD solver considers a finite element discretization of the balance of linear momentum and uses thin shell and Timoshenko beam formulations to define displacement interpolation functions.

The current paper proceeds as follows: the problem setup, including the ASPIRE geometries and relevant fluid and structural conditions, is outlined in Sec. II. The numerical methodologies for CFD, CSD, and FSI are presented in Sec. III. Simulation results, including comparison with flight data, are presented in Sec. IV. The computational cost of these simulations and conclusions are stated in Secs. V and VI, respectively.

II. Problem Description

The supersonic parachute inflation phase of the ASPIRE SR01 flight test is the problem of interest for the current simulation effort. In the SR01 flight test, a sounding rocket was used to launch a payload into the upper terrestrial atmosphere and accelerate it to supersonic speeds. Following this, a bag containing a build-to-print version of the MSL parachute was ejected from the rear of the payload. This bag convected downstream, and the parachute eventually escaped from the bag and inflated in $\approx 0.5s$ to a peak opening load of 30.95 klbf.[22] As opposed to the typical bluff-bodied entry capsules used in Martian landing missions, this flight test used a slender capsule, significantly reducing the interactions of the capsule wake with the bow shock that develops upstream of the canopy.[11,13,14]

A. Geometric Parameters

The total aerodynamic decelerator system consists of various sub-components that are labeled in Fig. 2: an 80 gore parachute canopy (comprised of the disk, gap, band, and vent hole) fabricated primarily from PIA-C-7020D nylon, 40 suspension lines crafted from 2100 lbf Technora cord, a riser, a triple bridle, and the slender payload.[22] The full dimensions are described in detail by O'Farrell *et al.*,[22] but some of the primary dimensions are summarized in Fig. 2 and Table 1.

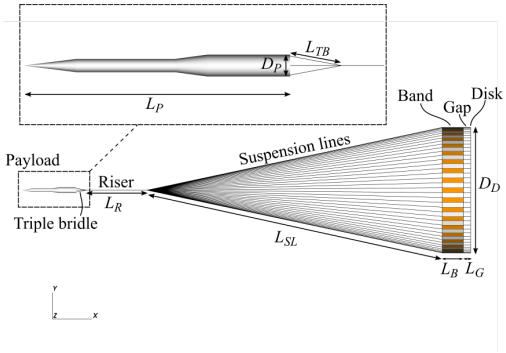


Figure 2: Aerodynamic decelerator system used in the ASPIRE SR01 flight test.

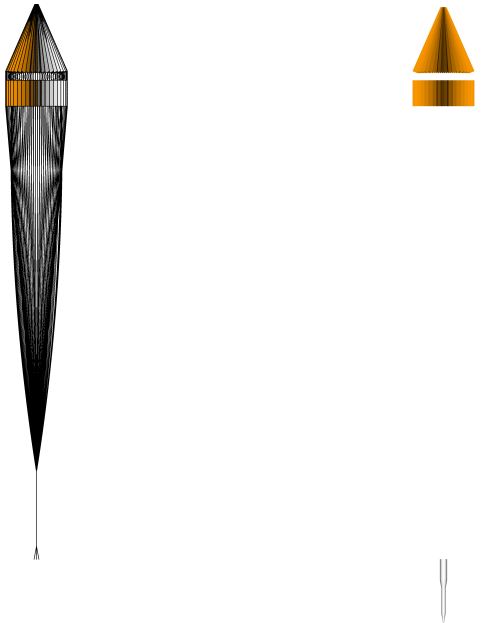
Unfolding and unpacking the parachute from the packed bag that is ejected from the trailing end of the payload is a computationally prohibitive and challenging task that is beyond the scope of this research, thus, the FSI simulations are started with initial conditions approximating the line stretch event. Line stretch occurs when the bag containing the parachute has convected downstream and the suspension lines first record tension. This event is typically used to signify the start of the inflation process.

To approximate the topology of the parachute at the line stretch event, the 'as-constructed' shape of the parachute in Fig. 2 is analytically folded/transformed into the 'umbrella' shape seen in Figs. 3a and 3b, shrinking the disk diameter from 15.44 m to 6.17 m. To preserve the length of the suspension lines, every other suspension line is defined as an arc rather than a straight line. Note that the suspension lines are not shown in Fig. 3b; the suspension lines are not immersed or modeled in the fluid domain and thus do not affect the fluid dynamics.

Table 1: Summary of key geometric parameters[22]

Parameter	Description	Value
D_0	Nominal diameter[a]	21.45 m
A_0	Nominal area	361.36 m^2
D_D	Disk diameter	15.44 m
L_G	Gap length	0.90 m
L_B	Band length	2.60 m
L_{SL}	Suspension line length	36.47 m
L_R	Riser length	7.5 m
L_{TB}	Triple bridle length	1.38 m
L_p	Payload length	6.66 m
D_p	Payload diameter	0.72 m
D_v	Vent hole diameter	1.50 m

[a] Note: the nominal diameter is conventionally the combined diameter of the disk, the gap, and the band.



(a) (b)

Figure 3: The initially folded (a) CSD mesh and (b) CFD geometry to be used in FSI simulations of the ASPIRE SR01 flight test.

B. Fluid Domain

The computational domain used in the present work ranges from $[-75, 75]$m $\times$ $[-50, 50]$m $\times$ $[-50, 50]$m and originates at the center of the leading edge of the folded disk. The farfield boundary conditions consist of a supersonic inlet boundary at $x = -75$ m, and all other boundaries are treated as extrapolation outflow boundaries. The block-structured Cartesian grid used in the fluid domain is shown in Fig. 4. The finest Cartesian grid level maintains an isotropic minimum grid spacing of $\Delta x_{min.} = 2.44$ cm and contains the capsule, the capsule wake, and the parachute canopy. AMR is used to track the motion of the parachute canopy with the finest grid level. The second finest level contains the bow shock upstream of the canopy and the immediate canopy wake. The freestream conditions are chosen to represent the line stretch event

during the ASPIRE SR01 flight test. Some freestream conditions were recorded by the on-board instrumentation: dynamic pressure, $q_\infty = 491.68$ Pa, Mach number, $M = 1.79$, and wind-relative velocity vector, $\mathbf{V}_f = (567.74, 0, 0)$ m/s at an altitude of 42.01 km,[22] but the freestream temperature is extracted from the reconstructed atmosphere profiles on the day of the launch as $T = 249.34$ K.[22]

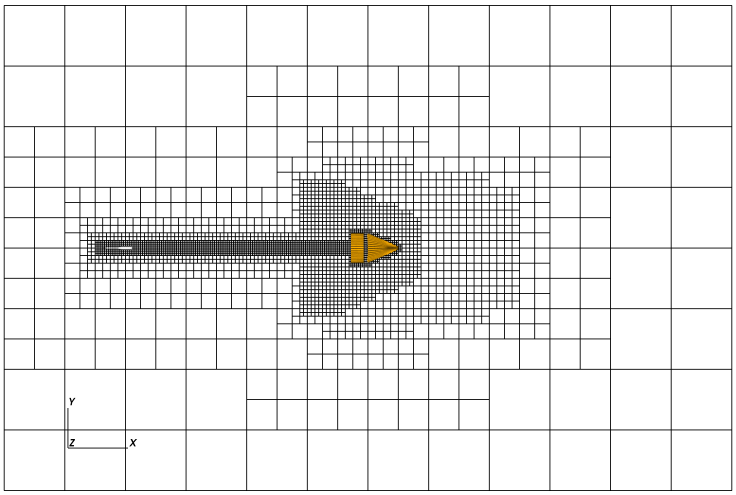


Figure 4: The ASPIRE geometries immersed into the initial block-structured Cartesian grid used in FSI simulations of the ASPIRE SR01 flight test. AMR is used to adapt the finest grid level to the parachute canopy during inflation. Each Cartesian block contains 16^3 grid cells.

C. Structural Domain

The structural mesh is shown in Fig. 3a. The parachute disk and band are discretized with $415k$ MITC3 triangular shell elements with an average edge length of $\approx 4\times10^{-2}$ m. The 40 suspension lines are constructed in a continuous fashion starting at the intersection of the riser and the suspension line confluent point, continuing through the canopy, across the vent hole, and back through the other side of the canopy before terminating again at the confluent point, thus there are effectively 80 suspension lines. Each effective suspension line is discretized with 200 Timoshenko beam elements from the leading edge of the band to the confluent point. Beam elements are also defined along the 80 radial seams in the parachute canopy and across the canopy gap and vent hole. The translational DOF at the leading end of the three bridles are fixed in space.

Note that the slender payload is rigid and static and is thus not considered in the CSD domain. The structural properties of the parachute system are summarized in Table 2.

Table 2: Summary of structural properties[23]

Parameter	Description	Value
E_c	Canopy elastic modulus	9.448×10^8 Pa
h_c	Canopy thickness	7.6073×10^{-5} m
ν_c	Canopy Poisson ratio	0.4
ρ_c	Canopy density	1154.25 kg/m^3
E_s	Suspension line elastic modulus	73.0×10^9 Pa
d_s	Suspension line diameter	3.175×10^{-3} m
ν_s	Suspension line Poisson ratio	0.4
ρ_s	Suspension line density	1154.25 kg/m^3

III. Methodology

A. Computational Fluid Dynamics (CFD)

1. *Interior Discretization*

The compressible Euler equations are discretized in space on a block-structured Cartesian grid with adaptive mesh refinement (AMR). The use of a block-structured Cartesian grid facilitates the construction of higher-order, conservative finite difference (FD) shock-capturing schemes.[24] Along these lines, the convective terms in the interior are discretized with a 5^{th}-order spatially accurate incremental-stencil[25] weighted essentially non-oscillatory (WENO-IS) scheme. While viscous effects are neglected in the interior discretization, they are modeled in the porosity boundary condition described in Sec. 3.

2. *Boundary Treatment*

Geometries are represented in a Lagrangian fashion as closed, or 'water-tight', surface triangulations. These triangulations are immersed into the background Cartesian mesh and are sharply represented by a ghost cell immersed boundary method (IBM), or ghost cell method (GCM).[26]

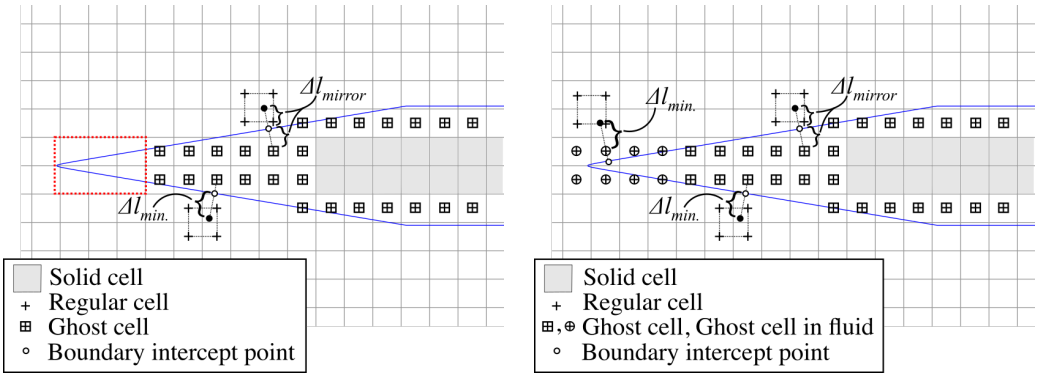


Figure 5: Ghost cell immersed boundary treatment using (a) conventional ghost cell method and (b) ghost cell in fluid method, both using a flexible mirror-image/fixed-distance approach. Note, with a conventional ghost cell method, the leading edge of the geometry in the red box would not be 'seen' or represented in the fluid domain due to insufficient volume resolution.

At the immersed boundary (IB), the solution of grid points one layer 'inside' of the geometry need to be filled appropriately – these are so-called ghost cells (see Fig. 5a). For treating thin geometries (with a thickness at or below the local volume grid spacing), however, a ghost cell-in-fluid (GIF) approach is used to define ghost cells outside of the geometry representation while maintaining a sharp representation of the immersed boundary.[27] This is illustrated on a cross-sectional slice of the leading edge of the ASPIRE payload in Fig. 5b. The state at both types of ghost cells, conventional and GIF, is filled by extending an interpolation point in a direction normal to the surface of the geometry ($\mathbf{n}$) and using the problem boundary conditions to formulate one-dimensional equations for each of the primary variables (*e.g.*, $\partial p/\partial \mathbf{n} = \partial T/\partial \mathbf{n} = 0$, for adiabatic non-porous walls with slip for velocity $\partial \mathbf{v}_{\tan}/\partial n = \mathbf{v} \cdot \mathbf{n} = 0$). The interpolation points are extended using mirror image distance across solid interface, Δl_{mirror}, when possible. If an explicit tri-linear interpolation stencil cannot be formed due to close proximity with the wall, the minimum fixed distance, $\Delta l_{min.}$, that does provide an explicit stencil is used.[27] Both of these scenarios are illustrated in Fig. 5.

3. *Solving the Darcy-Forchheimer Equation*

The stability of supersonic parachutes is a function primarily of porosity and Mach number,[28] thus, any computational FSI method considering high-fidelity parachute simulations must include a method for modeling the flow through a permeable canopy broadcloth. The thickness of parachute broadcloth is too thin to practically resolve ($76\mu m$), and thus, the conventional approach of applying a source term to grid points

within the porous medium cannot be used. Instead, the flow through a thin porous medium is modeled by representing a source term equation as a jump condition at the IB.

Considering the high Reynolds numbers experienced during supersonic parachute flight, the Forchheimer correction form of Darcy's law, or the Darcy-Forchheimer equation is considered. A closed-form solution to the Darcy-Forchheimer momentum equation is derived and written in terms of the mass flux, q,

$$q = \rho_1 v_{n,1} = \rho_2 v_{n,2} = -\frac{1}{2K_p\beta}\left(\mu(\bar{T}) - \sqrt{\frac{2K_p^2\beta(p_2^2 - p_1^2)}{WR\bar{T}} + \mu(\bar{T})^2}\right), \tag{1}$$

where $\bar{T} = 1/2(T_1 + T_2)$, $p_2 > p_1$, W is the width of the porous medium, and the subscripts 1 and 2 refer to a state of the fluid on either side of the porous medium. In practice, these states are sampled by the IBM and an additional, reflected interpolation point that is extended into the volume using $-\mathbf{n}$ (see Fig. 6). The typical slip or no-slip velocity boundary conditions at the IB are then modified by adding a wall-normal component to the velocity given by $v_{n,1} = q/\rho_1$ or $v_{n,2} = q/\rho_2$, depending on which side of the IB the ghost cell in question is on.

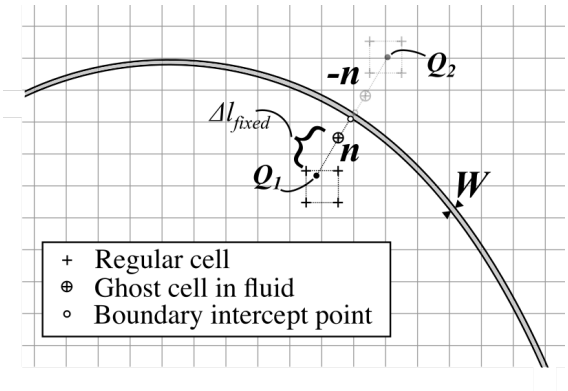


Figure 6: Schematic of the porous immersed boundary treatment for a thin geometry. The reflected boundary intercept, interpolation point, and tri-linear stencil are shaded in light grey.

Values of K_p and β are determined empirically from experimental data gathered by Cruz *et al.*[29] studying the permeability of PIA-C-7020D Type I nylon - the same material used to construct the canopy used during the ASPIRE SR01 flight test. Using the analytical expression in Eq. (1) and the experimental results, values are determined for the permeability coefficient, $K_p = 8.5 \times 10^{-12}$ m^2, and the inertial permeability coefficient, $\beta = 1.9 \times 10^6$ 1/m, by assuming a material thickness of $W = 7.6073 \times 10^{-5}$ m.[23]

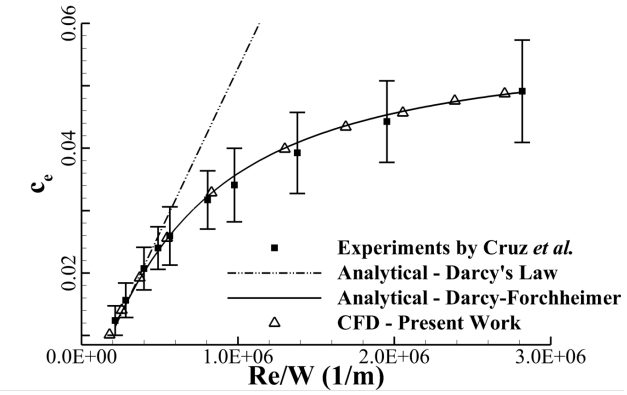


Figure 7: The effective porosity of PIA-C-70270D broadcloth recorded as a function of the unit Reynolds number from experiments and predicted via analytical (Eq. 1) and computational approaches.

The analytical expression in Eq. (1) and the conventional Darcy's law are then completed with the empirically determined coefficients and compared against the experimental data in Fig. 7. Also shown are the results from CFD simulations that include the porous immersed boundary condition, a porous medium of width 7.6073×10^{-5} m in the center of a 2D channel (with periodic top and bottom boundaries and subsonic outflow boundaries at the left and right domain edges), and varying pressure gradients, Δp, defined across the porous medium. The plotted quantities are the effective porosity, $c_e = q/(\rho V)$ (V is the fictitious freestream given by $\sqrt{2\Delta p/\rho}$), and the Reynolds number per unit width of the porous medium, Re/W.[29] The analytical porosity model and its CFD implementation show good agreement with the experimental data.

B. Computational Structural Dynamics (CSD)

1. Element Selection

The CFD solver is coupled to a geometrically nonlinear structural dynamics solver that is used to simulate the unsteady response of thin shell and cable/beam structures relevant for parachute inflation. The structural solver employs the finite element method to discretize the balance of linear momentum in the structural domain.

The parachute canopy uses MITC3 3-node, triangular shell elements[30,31] to define the interpolation functions and strain-displacement relationships. The MITC3 shell element employs the mixed interpolation of tensorial components (MITC) scheme to alleviate shear locking in bending dominated problems.[32] To capture the complex starting conditions described in Sec. II, with shell elements starting at sharp angles with one another, a 6 degree-of-freedom (DOF) formulation of the MITC3 element is used. The zero pivot corresponding to the in-plane rotation in the element local system, or the 'drilling' DOF, is treated with a drilling stiffness, K_{drill}. The drilling stiffness is defined by some factor, $c_{drill.}$,

$$K_{drill.} = c_{drill.} \cdot \min(K_{trans._1}, K_{trans._2}), \tag{2}$$

where $K_{trans._1}$ and $K_{trans._2}$ represent the two 'natural' components of transverse shear stiffness in the local system. Suitable choices for c_{drill} vary, but a value of 10^{-2} is used throughout this paper.

The suspension lines are discretized with curved, 6 DOF Timoshenko 2-node beam elements.[33] To alleviate shear locking, reduced integration is performed along the length of the element. Slack, or zero resistance to compressive axial forces in the suspension lines, is enforced in the local system by

$$S_{axial} = C_{axial} \cdot \max(E_{axial}, 0), \tag{3}$$

where S_{axial} represents the axial component of the second Piola-Kirchhoff stress tensor, C_{axial} is the axial component of the local constitutive matrix, and E_{axial} is the axial component of the Green-Lagrange strain tensor.

C. CFD-CSD Coupling

The CFD and CSD solvers interact through the transmission of loads and displacements across their shared domain boundary. In practice, this shared domain boundary is the finite thickness, zero-mass surface triangulation representing the CFD geometry. The infinitesimal thickness CSD mesh lies on the mid-plane of the CFD geometry. Methods introduced by Boustani *et al.*[34] to transfer velocities and tractions across such an interface are employed in this work.

Given the large fluid-to-structure density ratios present in supersonic parachute inflation, which typically occurs at very high altitudes, the CFD and CSD solvers are coupled in time in a loose fashion. In this loose coupling approach, the CFD time integration, which uses a 2$^{\text{nd}}$-order temporally accurate, explicit strong-stability preserving Runge-Kutta (SSP-RK) scheme, advances the CFD solver as normal, and at every SSP-RK sub-step with a time-level update, the CSD solver, using a 2$^{\text{nd}}$-order temporally accurate, explicit central difference method, is called, and the geometry is deformed accordingly. At the end of the full timestep, the aerodynamic tractions are transferred from the surface of the CFD geometry to the CSD mesh along with any penalty contact tractions.

Given the multi-physical nature of the problem, it is possible that one solver may experience a more restrictive explicit timestep than the other at any given time. In fact, the CSD solver typically has a stable timestep that is approximately an order of magnitude smaller than the stable timestep in the CFD solver. To

avoid running the more costly CFD solver at this unnecessarily small timestep, the CSD solver is sub-cycled, and each time the CSD solver is called, it advances N_{cycles} sub-cycles with a timestep of $\widetilde{\Delta t}_{CSD}$. These variables are defined by

$$N_{cycles} = \text{ceil}\left(\frac{\Delta t_{CFD}}{\Delta t_{CSD}}\right) \tag{4}$$

and

$$\widetilde{\Delta t}_{CSD} = \frac{\Delta t_{CFD}}{N_{cycles}}, \tag{5}$$

respectively, where Δt_{CFD} and Δt_{CSD} are the largest stable timesteps for the CFD and CSD solvers, and $\widetilde{\Delta t}_{CSD}$ is the sub-cycled CSD timestep.

1. *Contact Identification and Enforcement*

In order to consider the folded canopy topology presented in Sec. II, a virtual contact identification and penalty forcing strategy inspired by Boustani *et al.*[35] is employed in the present work with some modifications. The concept of 'virtual' contact ensures that contact is identified before two bodies actually intersect. Once identified, contact is enforced some distance off of the surfaces. This is required during FSI simulations to avoid collapsing or generating cells with negative volume with Arbitrary Lagrangian Eulerian approaches[17] or interfering with the geometry queries in an IB framework, which rely on a water-tight, closed representation of the geometry.

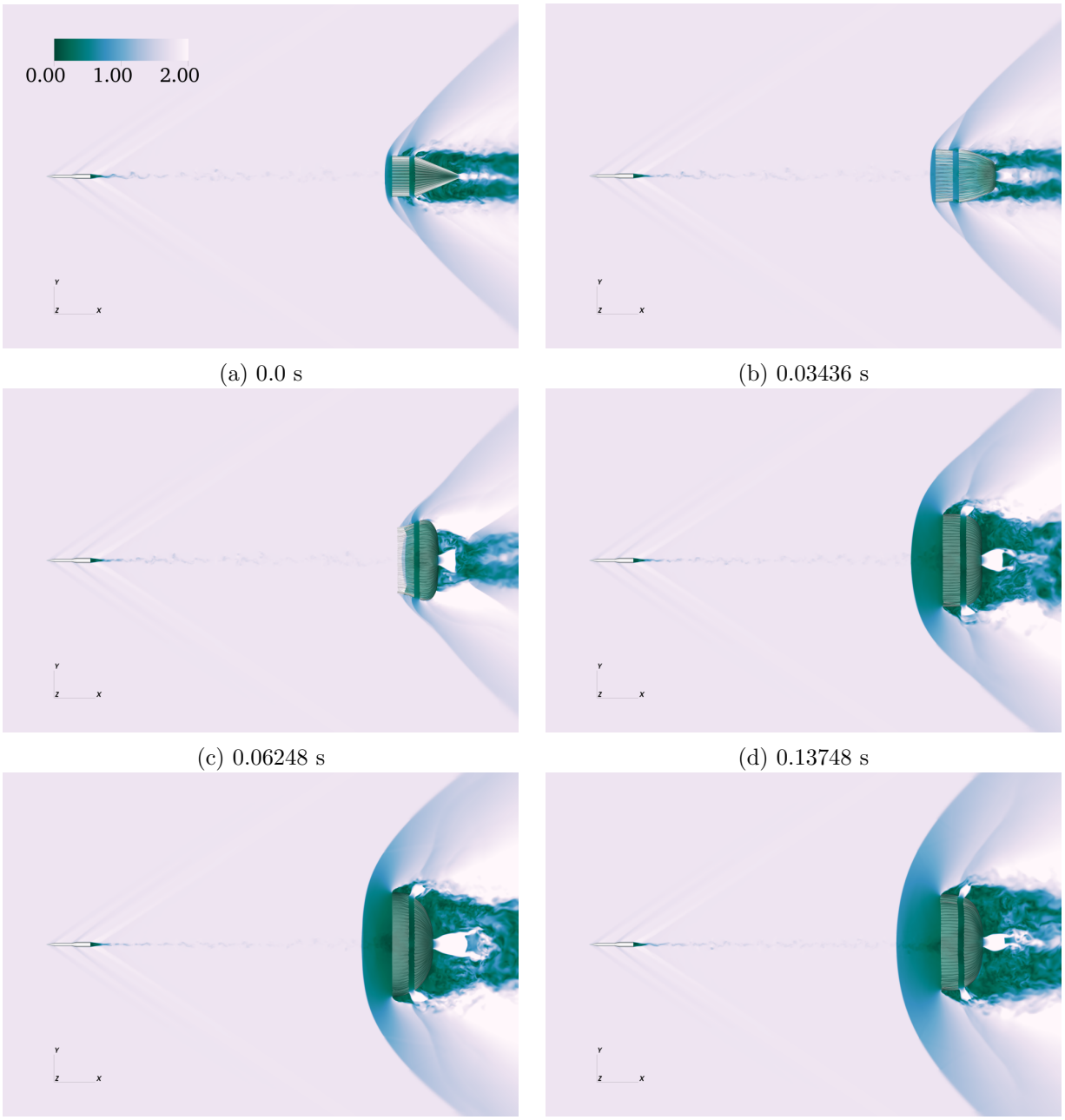
In the current work, contact is identified between two closely located discrete elements that compose the CFD geometry mesh using optimized ray-tracing algorithms.[36] The result of this ray-tracing step is a contacting pair of discrete triangles. The enforcement strategy used by Boustani *et al.*,[35] where a penalty impulse is generated by the change in momentum of the two contacting triangles, is directly employed here. The virtual contact 'gap', or the distance off the surfaces that contact is identified and enforced at, is set in this work to be 4 times the minimum volume grid spacing, $\Delta x_{min.}$, in the surrounding fluid domain.

IV. Results

The supersonic parachute inflation phase from the ASPIRE SR01 flight test is simulated with FSI over the time interval [0.0 s, 0.475 s]. During this interval, the rise in loading, peak opening load, canopy rebound, and a gradual recovery are expected to be observed. In the flight tests, a load pin was placed at the leading edge of each leg in the triple bridle, and when summed together, these load pins provide the total pull force experienced by the parachute. For comparison, a similar metric is recorded in the FSI simulations conducted here: the restoring force in the beam elements at the leading edge of each leg in the triple bridle. All FSI simulations begin with a precursor CFD-only simulation conducted over rigid and static versions of the ASPIRE geometries until the primary flow features are developed and the loads on the parachute canopy become statistically stationary. Once this occurs, the simulation is restarted with this flow field, now considering the coupled fluid-structural dynamic response.

Figs. 8a-8f show the Mach number in the flow field around the inflating parachute canopy at six instances in time during the inflation process. In Fig. 8b, the band and disk are beginning to react to the high pressure flow in the canopy and are expanding outward. By Fig. 8c, the disk appears to be fully inflated while the band begins to lag in the inflation process. Qualitatively, this is consistent with the ASPIRE flight test, where the disk area dominated the total drag area of the canopy at peak loading.[22] Fig. 8d shows the canopy at the instance of the peak opening load, and similar to the flight tests, the peak load occurs just before the full inflation of the parachute canopy. In Fig. 8e, the canopy has rebounded from the peak opening load and has moved slightly upstream, causing the canopy bow shock to flatten and more flow to accelerate through the vent hole. By Fig. 8f, the parachute is fully inflated but is still subject to interaction with its turbulent wake and over-pressurization in the canopy. To highlight the wide range of densities that occur throughout this process, snapshots of the logarithm of density are also shown in Figs. 9a-9f.

Slices of the leading edge of the parachute band at the same instances in time are visualized in Fig. 10. The inflation is largely symmetric, with asymmetries occurring on a very small scale between the radial



(a) 0.0 s

(b) 0.03436 s

(c) 0.06248 s

(d) 0.13748 s

(e) 0.18123 s

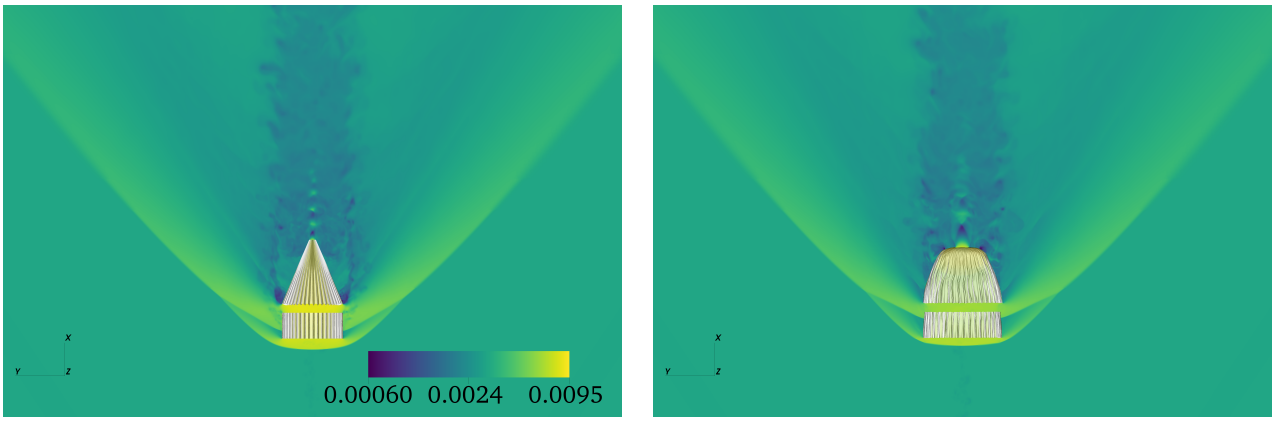
(f) 0.40623 s

Figure 8: (a)-(f) Saturated pseudocolor contours of Mach number shown on a cut-plane through the center of the domain at six instances in time during the inflation process.

seams. At the point of over-expansion and maximum area (orange), the small-scale surface features have been virtually removed as the parachute broadcloth is stretched taut.

Fig. 11 shows the time history of the total pull force predicted by the current FSI simulations and those recorded by the load pins during the ASPIRE flight test. A quicker rate of loading is predicted in the current simulations, but the predicted peak load of 34.1 klbf is within 10% of the recorded peak load in flight data (note that the load pins had a measurement uncertainty of 3.3% at the instance of peak loading). This slight overshoot causes an excessive rebounding around 0.09 s, but a similar rate of recovery between 0.09 s and 0.3 s is observed.

A few assumptions that have so far been made can now be evaluated. The folded starting topology is an



(a) 0.0 s

(b) 0.03436 s

(c) 0.06248 s

(d) 0.13748 s

(e) 0.18123 s

(f) 0.40623 s

Figure 9: (a)-(f) Zoomed in views of saturated pseudocolor contours of the logarithm of density (kg/m^3) shown on a cut-plane through the center of the domain at six instances in time during the inflation process.

idealized representation of the parachute canopy at line stretch, and this idealized representation starts the simulations with a non-zero projected area. This initial projected area speeds up the inflation process, likely the cause of the quicker rate of loading from the start of the simulation to peak load. In addition, the flow conditions are 'frozen' throughout the simulation, and the total parachute system is fixed at the capsule and does not decelerate like the flight test.[22] Finally, no attempt is made to simulate or model the canopy being packed into a bag and ejected from the back of the payload or the effect of the suspension lines on the flow field, and the effect this may have on the opening dynamics and peak load is unclear.

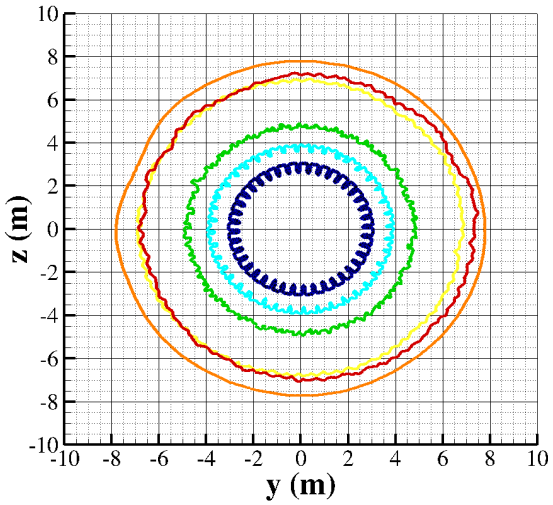


Figure 10: Positions of nodes on the leading edge of the band in the CSD mesh projected into the $y-z$ plane at each of the 6 snapshots from Figs. 8 and 9. Time advances from blue (0.0 s), teal, green, yellow, orange, and red (0.40623 s).

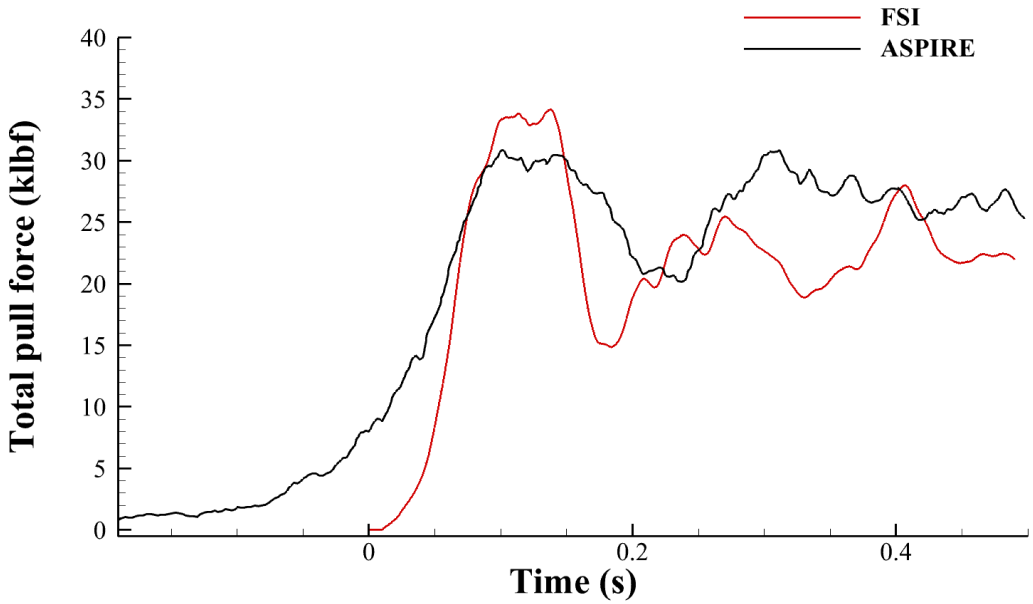


Figure 11: Time history of the total pull force predicted by the current FSI simulation and recorded during the ASPIRE flight test. Note that due to the idealized line stretch geometry, the simulated inflation times will not exactly match the flight test, so the flight test data is shifted along the x-axis for comparison.

Despite these limitations, to the best of the author's knowledge, these are the first FSI simulations to reproduce and compare with the ASPIRE flight data, and the current FSI method predicts a peak opening load within 10% of the flight data. The general characteristics of the load profile: the rise, peak, rebound, and recovery, are all qualitatively similar to the flight test data.

In order to quantify the effect of spatial discretization error on the value of the peak opening load, Sec. A studies the sensitivity of the peak opening load and other metrics to the spatial resolution in the volume

and structural domains.

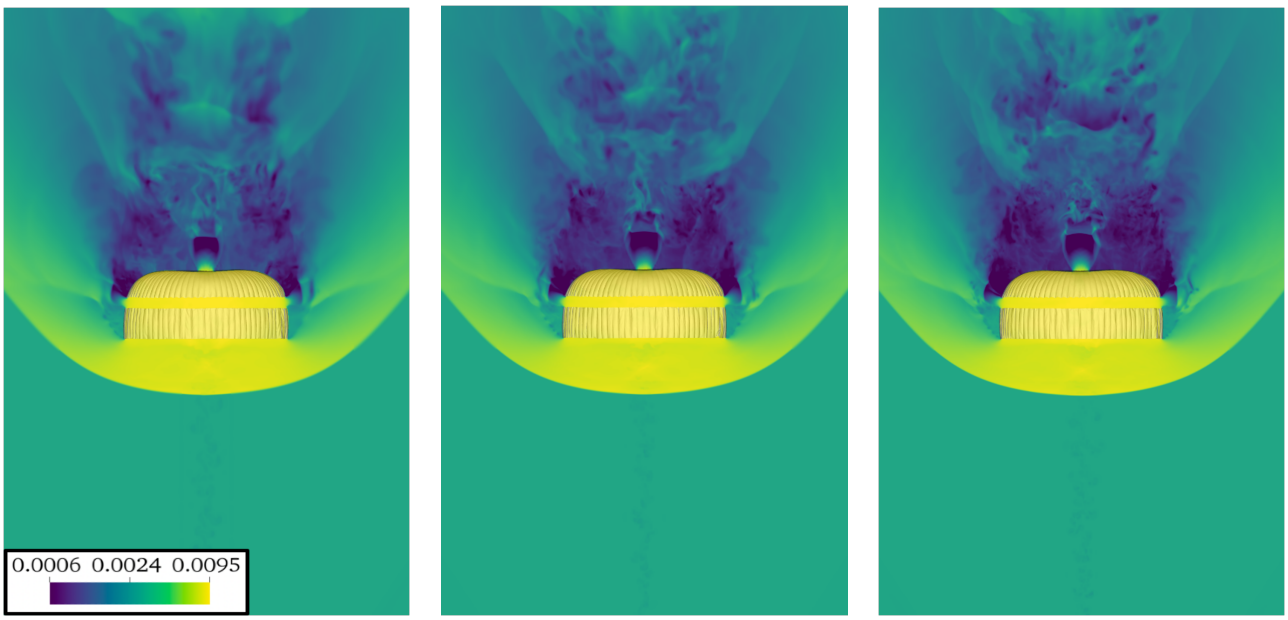
A. Grid Convergence Study

1. Solution Sensitivity to Volume Grid Resolution

The grid considered in the baseline simulation with a minimum spacing of $\Delta x_{min.} = 2.44$ cm is coarsened and refined by a factor of approximately $2^{1/3}$ across the entire domain to create 'coarse' and 'fine' grids. The parameters for each grid are summarized in Table 3. Note that the N_{cells} presented in Table 3 is from the initial grid layout, and during the course of a simulation, as the finest level of mesh adapts to track the geometry, this may increase by at least 10%. For the new cases, the flow field is again developed over the static and rigid canopy and capsule, and subsequently, the time interval [0.0 s, 0.475 s] is simulated with FSI.

Table 3: Parameters for the ASPIRE FSI CFD Grid Convergence Study

Grid	$\Delta x_{min.}$ (cm)	N_{cells} ($\times 10^6$)
Coarse	3.25	128
Medium	2.44	226
Fine	1.95	400

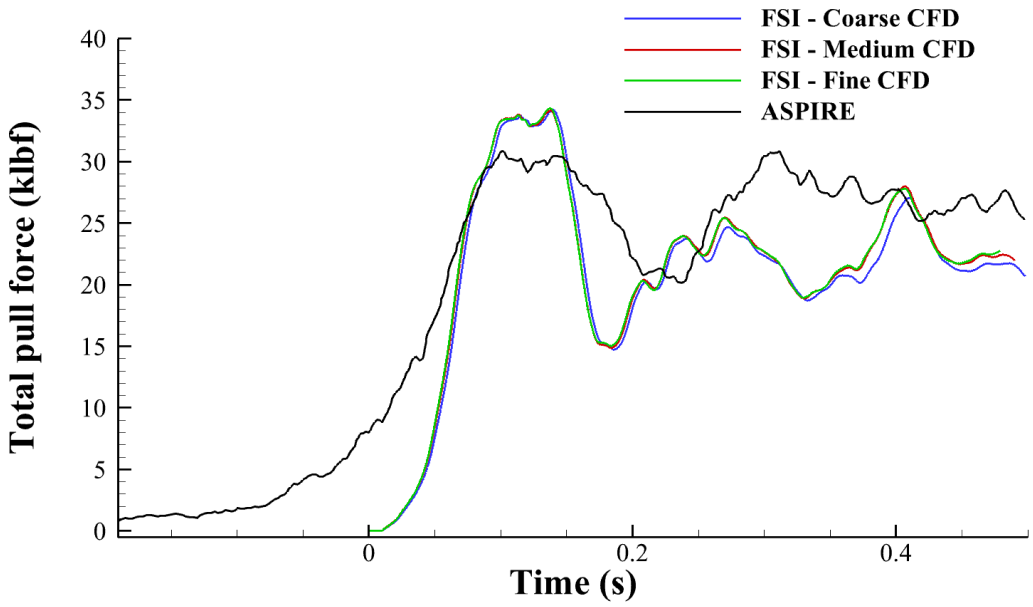


(a) Coarse (b) Medium (c) Fine

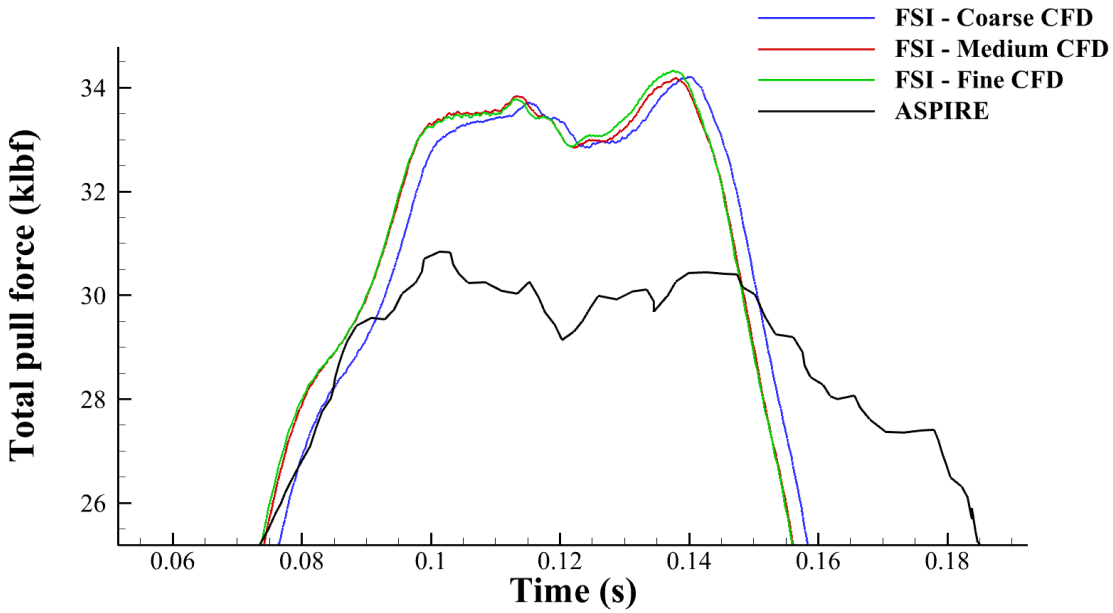
Figure 12: (a)-(c) Saturated pseudocolor contours of the logarithm of density (kg/m^3) at the instance of peak loading for each grid considered in the ASPIRE FSI grid convergence study.

Figs. 12a-12c show the logarithm of density at the instance of peak loading for each volume grid resolution. As the grid is refined, small-scale features are resolved in the wake of the canopy, *e.g.,* small vortices rolling off the leading edge of the band can be observed clearly in Fig. 12c. Qualitatively, the bow shock shape, the width of the canopy wake, and the topology of the recompression shock in the canopy wake are all similar. This is quantitatively shown in Fig. 13, where the time history of the total pull force for each simulation is plotted with the flight data.

In Fig. 13a, the coarse CFD grid can be seen to slightly deviate from the medium and fine grids after approximately 0.3 s, but the rate of initial loading, peak load, and rebound are very similar for all three grids. In fact, Fig. 13b shows a zoomed in view of the time histories around the instance of peak loading,



(a)



(b)

Figure 13: (a) Full and (b) partial time histories of the total pull force predicted by the three FSI simulations in the ASPIRE FSI grid convergence study and recorded during the ASPIRE flight test.

and all three grids predict a peak load within 1% of each other. Thus, we can conclude that the total pull force is converging (see Table 4) and that the spatial discretization at these resolutions is sufficient (less than 1% difference in the quantities of interest) and is not affecting the shape of the total pull force versus time curve. This is a significant finding that is rarely reported in this field. We hope this will motivate other authors to conduct such studies in the future.

Furthermore, this analysis can be expanded on by interpolating the coarse and medium time signals onto the fine time signal and computing the absolute difference in the total pull force from the coarse-to-medium

and medium-to-fine grids - this is shown in Fig. 14. Convergent behavior can be observed as the solution difference between the coarse and medium meshes is $\approx 4.6\times$ larger than the mean difference between the medium and fine meshes over the total simulated time interval [0.0 s, 0.475 s].

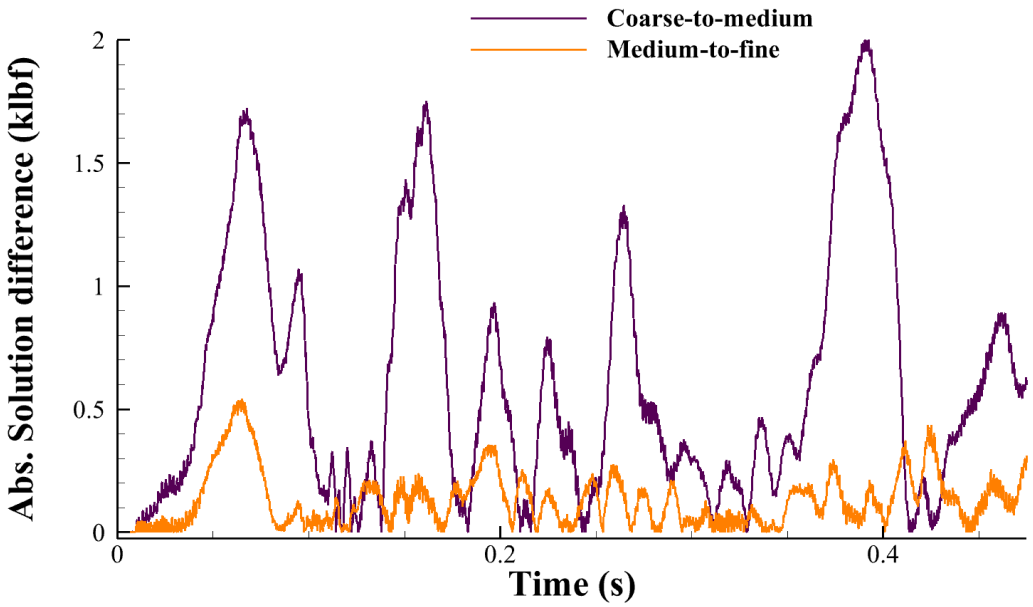


Figure 14: Time history of the absolute difference in the coarse and medium grid and medium and fine grid total pull forces from the ASPIRE FSI grid convergence study.

This simulated time interval contains the transient inflation process and is by no means statistically stationary. An attempt is still made, however, to further quantitatively analyze the convergence behavior of the solutions with respect to the volume domain resolution using a variety of metrics. Furthermore, because the primary quantity of interest in supersonic parachute inflation is the peak opening load, quantities of interest are considered over smaller time interval of [0.095 s, 0.145 s] that strictly contains the 'plateau' region of the pull force and the peak loading.

The total pull force for each simulation is both averaged and integrated in time over this interval to obtain a measure of the mean peak load and the peak impulse. Table 4 summarizes the grid-convergence-index (GCI), estimated converged values, and the estimated uncertainties computed using standard ASME procedures.[37] Very low grid-related uncertainty is shown ($< 0.15\%$ for both metrics), and grid convergence has been demonstrated.

Table 4: Summary of ASPIRE FSI CFD Grid Convergence Study

Metric	Coarse	Medium	Fine	GCI[37]	Est. Converged Value	Est. Uncertainty
Peak Load (klbf)	33.2653	33.3620	33.3979	0.0014856	33.4255	±0.047142
Peak Impulse (klbf·s)	1.6629	1.6679	1.6696	0.0013108	1.6707	±0.002190

If a convergence rate is computed from the data in Table 4, a higher-order value of approximately 4 is observed. While this higher-order convergence rate likely does not reflect the order of the underlying numerical method, a positive value implies that the solutions are converging regardless. In addition, this implies that the temporal error does not dominate the solution. Had this been the case, the convergence rate of all metrics would have been limited to 1$^{\text{st}}$- or 2$^{\text{nd}}$-order, corresponding to the temporal order of accuracy of the coupled FSI method or the time integration scheme used in each domain.

For completeness, the metrics used to analyze the convergence behavior over the inflation time interval were also considered over the total simulated time interval of [0.0 s, 0.475 s]. The GCI for all metrics and

both time intervals, however, is always less than 0.5%. The convergent behavior of the method over the total time interval is evident in Fig. 14. The insensitivity of the solution to the volume grid resolution also indicates that further refinement will not yield better agreement with the flight test data. To remove the possibility of discretization error in the structural domain being the cause of this systematic error, the following sub-section considers a final FSI simulation using a refined CSD and geometry surface mesh.

2. Solution Sensitivity to Structural Mesh Resolution

Similar to the volume grid resolution study, the structural mesh resolution study will consider refinement factors of approximately $2^{1/3}$ applied to the average edge length, $\Delta l_{avg.}$, for consistency. To start, only one finer structural mesh is considered - it is expected that the sensitivity of the peak opening load to the resolution in the CSD will be small. For identification purposes, the CSD mesh used in the three previous FSI simulations will be termed 'medium', and the finer mesh will be termed 'fine'. The parameters of the medium and fine CSD meshes are summarized in Table 5.

Table 5: Parameters for the ASPIRE FSI CSD Grid Convergence Study

Grid	$\Delta l_{avg.}$ (cm)	$N_{elem.}$ ($\times 10^3$)	N_{nodes} ($\times 10^3$)	N_{DOF} ($\times 10^6$)
Medium	4.09	415	210	1.26
Fine	3.15	738	372	2.22

Similar procedures are used to establish the flow field and begin the FSI simulations, where the time interval of [0.0 s, 0.475 s] is simulated using the medium CFD grid and fine CSD mesh. The total pull force predicted by the medium CFD - medium CSD and the medium CFD - fine CSD grids are shown in Fig. 15a along with the differences in the total pull forces for all simulations in Fig. 15b. Again, there is less than 1% difference in the magnitude of the predicted peak opening loads between the CSD meshes, and the differences in pull force over the total simulation interval for the CSD meshes is comparable to the differences between the CFD grids.

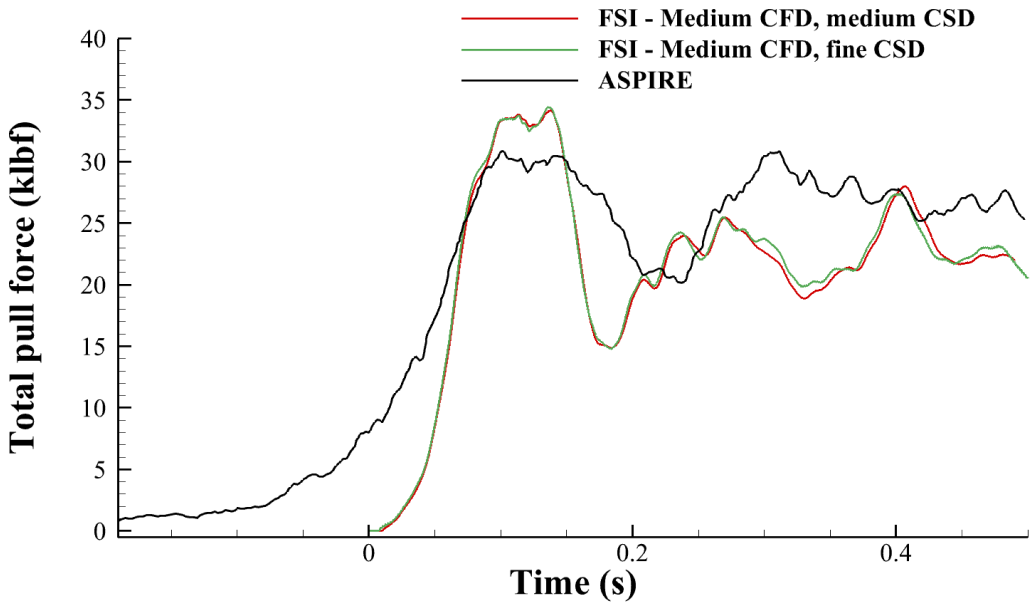
Thus, the solution remains insensitive to increasing grid resolution, whether it be in the CSD or CFD domains. This is in itself a significant finding. The uncertainty due to discretization errors has been carefully bounded, and it can be stated confidently that the remaining error is due to modeling deficiencies and not discretization errors. A high degree of repeatability has been demonstrated. Despite the modeling deficiencies, the method predicts the peak opening load within 10% of the flight data, a margin certainly within acceptable engineering-level predictions.

V. Computational Resources

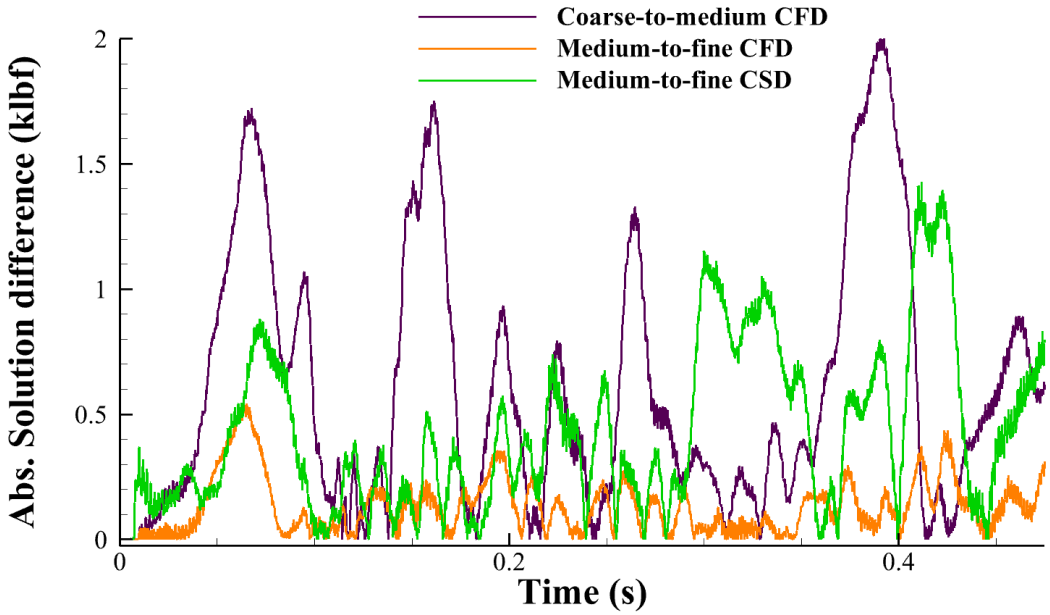
In a practical use case for engineers, a wide-range of simulations covering various freestream and initial conditions, parachute geometries, and even structural properties may need to be considered. This is only possible if the turn-around time fits within the project's schedule and computational resources for each simulation are available and fit within the project's budget. Significant effort has been placed in the computational efficiency of the current FSI method. The computational resources required by the FSI simulations conducted in this paper are summarized in Table 6. All simulations were conducted on Cascade Lake nodes and NASA Advanced Supercomputing (NAS) systems. The core-hours are shown in the right-most column of Table 6. Following the grid convergence analysis, it can be concluded that the Coarse CFD - Med. CSD simulation may be sufficient to predict the peak opening load and general post-inflation dynamics. Thus, a single simulation can be conducted on modest resources of about 1600 cores in less than 36 hours. If the duration of the simulation needed to be lowered, the strong scaling performance of the FSI method would permit additional cores to be used efficiently and the turnaround time would likely be lowered.

VI. Conclusions

The Launch, Ascent, and Vehicle Aerodynamics (LAVA) Cartesian CFD and finite element CSD solvers were used to simulate the supersonic parachute inflation phase of the ASPIRE SR01 flight test with fluid-



(a)



(b)

Figure 15: Time history of the (a) total pull force and (b) total pull force differences between CFD and CSD grids with various levels of refinement.

structure interaction (FSI). The methodologies for immersing thin, complex geometries in a block-structured Cartesian grid with a ghost-cell method (GCM) were summarized, and the finite elements used in the CSD solver were discussed. The CFD and CSD solvers were loosely coupled in space through the exchange of motion and loads across a surface triangulation representing the shared domain boundary and in time through an explicit/explicit CFD/CSD time integration strategy with the possibility to sub-cycle the CSD solver.

FSI simulations were conducted at multiple volume grid resolutions to study the grid sensitivity of the

Table 6: Summary of Computational Resources Used in ASPIRE FSI Simulations

Simulation	N_{cores}	Duration (hours)	Resources (core-hours)
Coar. CFD - Med. CSD	1600	32	51,200
Med. CFD - Med. CSD	960	67	64,320
Fine CFD - Med. CSD	2400	70	168,000
Med. CFD - Fine CSD	2400	58	139,200

peak opening load. The peak loads predicted by each grid resolution varied by less than 1% from one another and was within 10% of the flight data. The grid-related uncertainty was quantitatively shown to be very low ($< 0.15\%$). Multiple metrics were used to estimate the convergence rate of the solutions, and a rate of approximately 4 was computed. While not necessarily indicative of the underlying numerical schemes, it does imply that the temporal error (1^{st}- or 2^{nd}-order) does not dominate the solution. Following this, the resolution of the structural and geometry meshes were refined, and again, the peak load was predicted within 1% of the previous simulations. To the best of the author's knowledge, these are the first simulations to reproduce and compare with the ASPIRE SR01 flight test.

The systematic 10% difference between the predicted opening load and the flight data is attributed to modeling deficiencies. These range from possibly not properly representing the complicated initial fluid-structural state to not simulating the deceleration of the total parachute system, or material modeling and other factors not yet considered. These items will be investigated in the future in order to increase confidence in the accuracy of these simulations and provide a useful tool to engineers studying the Entry, Descent, and Landing process (EDL).

Finally, the required computational resources were documented, and it was shown that using a modest amount of cores, a simulation can be conducted in less than 36 hours. With further code optimizations and taking advantage of the strong scaling characteristics of the solver, larger parametric studies studying sensitivity to fluid conditions (Mach number, altitude, angle of attack) and material properties may soon be within reach.

VII. Acknowledgments

This work was partially supported by the NASA Entry Systems Modeling (ESM) project and the NASA Transformational Tools and Technologies (T^3) project. Computational resources were provided by NASA Advanced Supercomputing (NAS) systems at NASA Ames Research Center. C. Brehm greatly acknowledges funding from the Computational Aerosciences Branch at NASA Ames Research center.

References

[1]Clark, I. and Tanner, C., "A historical summary of the design, development, and analysis of the disk-gap-band parachute," *2017 IEEE Aerospace Conference*, IEEE, 2017, pp. 1–17.

[2]Sengupta, A., Steltzner, A., Witkowski, A., Candler, G., and Pantano, C., "Findings from the supersonic qualification program of the Mars Science Laboratory parachute system," *20th AIAA aerodynamic decelerator systems technology conference and seminar*, 2009, p. 2900.

[3]Gallon, J., Witkowski, A., Clark, I. G., Rivellini, T., and Adams, D. S., "Low density supersonic decelerator parachute decelerator system," *AIAA Aerodynamic Decelerator Systems (ADS) Conference*, 2013, p. 1329.

[4]Way, D. W., Powell, R. W., Chen, A., and Steltzner, A. D., "Asymptotic parachute performance sensitivity," *2006 IEEE Aerospace Conference*, IEEE, 2006, pp. 9–pp.

[5]Clark, I. G., Gallon, J. C., and Witkowski, A., "Parachute Decelerator System Performance During the Low Density Supersonic Decelerator Program's First Supersonic Flight Dynamics Test," *23rd AIAA Aerodynamic Decelerator Systems Technology Conference*, 2015, p. 2130.

[6]Clark, I. G., Manning, R., and Adler, M., "Summary of the First High-Altitude, Supersonic Flight Dynamics Test for the Low-Density Supersonic Decelerator Project," *23rd AIAA Aerodynamic Decelerator Systems Technology Conference*, 2015, p. 2100.

[7]"Third ASPIRE Test Confirms Mars 2020 Parachute a Go," *NASA*, October 2018, pp. https://www.nasa.gov/feature/jpl/third–aspire–test–confirms–mars–2020–parachute–a–go.

[8]Karagiozis, K., Kamakoti, R., Cirak, F., and Pantano, C., "A computational study of supersonic disk-gap-band parachutes

using Large-Eddy Simulation coupled to a structural membrane," *Journal of Fluids and Structures*, Vol. 27, No. 2, 2011, pp. 175–192.

[9]Gidzak, V., Nompelis, I., Candler, G., Barnhardt, M., Drayna, T., and Garrard, W., "Comparison of Fluid-Structure Interaction Simulations of the MSL Parachute With Wind Tunnel Tests," *20th AIAA aerodynamic decelerator systems technology conference and seminar*, 2009, p. 2971.

[10]Barnhardt, M., Drayna, T., Nompelis, I., Candler, G., and Garrard, W., "Detached eddy simulations of the MSL parachute at supersonic conditions," *19th AIAA Aerodynamic Decelerator Systems Technology Conference and Seminar*, 2007, p. 2529.

[11]Muppidi, S., O'Farrell, C., Van Norman, J., and Clark, I., "Simulations of Wakes and Parachute Environments for Supersonic Flight Test Design," *APS Division of Fluid Dynamics Meeting Abstracts*, 2017, pp. L30–004.

[12]O'Farrell, C., Muppidi, S., Brock, J. M., Van Norman, J. W., and Clark, I. G., "Development of models for disk-gap-band parachutes deployed supersonically in the wake of a slender body," *2017 IEEE Aerospace Conference*, IEEE, 2017, pp. 1–16.

[13]Muppidi, S., O'Farrell, C., Tanner, C., Van Norman, J. W., and Clark, I. G., "Modeling and Flight Performance of Supersonic Disk-Gap-Band Parachutes in Slender Body Wakes," *2018 Atmospheric Flight Mechanics Conference*, 2018, p. 3623.

[14]Muppidi, S., O'Farrell, C., Van Norman, J. W., and Clark, I. G., "ASPIRE Aerodynamic Models and Flight Performance," *AIAA Aviation 2019 Forum*, 2019, p. 3376.

[15]Gao, X., Zhang, Q., and Tang, Q., "Numerical modelling of Mars supersonic disk-gap-band parachute inflation," *Advances in Space Research*, Vol. 57, No. 11, 2016, pp. 2259–2272.

[16]Sengupta, A., Wernet, M., Roeder, J., Kelsch, R., Witkowski, A., and Jones, T., "Supersonic testing of 0.8 m disk gap band parachutes in the wake of a 70 deg sphere cone entry vehicle," *20th AIAA Aerodynamic Decelerator Systems Technology Conference and Seminar*, 2009, p. 2974.

[17]Xue, Y., Li, Y., Min, L., and Haofei, P., "Fluid structure interaction simulation of supersonic parachute inflation by an interface tracking method," *Chinese Journal of Aeronautics*, Vol. 33, No. 6, 2020, pp. 1692–1702.

[18]Yang, X., Yu, L., Nie, S., and Zhang, S., "Aerodynamic performance of the supersonic parachute with material permeability," *Journal of Industrial Textiles*, Vol. 50, No. 6, 2021, pp. 812–829.

[19]Yu, H., Pantano, C., and Cirak, F., "Large-Eddy Simulation of Flow Over Deformable Parachutes using Immersed Boundary and Adaptive Mesh," *AIAA Scitech 2019 Forum*, 2019, p. 0635.

[20]Huang, Z., Avery, P., Farhat, C., Rabinovitch, J., Derkevorkian, A., and Peterson, L. D., "Simulation of parachute inflation dynamics using an Eulerian computational framework for fluid-structure interfaces evolving in high-speed turbulent flows," *2018 AIAA Aerospace Sciences Meeting*, 2018, p. 1540.

[21]Borker, R., Huang, D., Grimberg, S., Farhat, C., Avery, P., and Rabinovitch, J., "Mesh Adaptation Framework for Embedded Boundary Methods for CFD and Fluid-Structure Interaction," *International Journal for Numerical Methods in Fluids*, 2019.

[22]O'Farrell, C., Karlgaard, C., Tynis, J. A., and Clark, I. G., "Overview and reconstruction of the ASPIRE project's SR01 supersonic parachute test," *2018 IEEE Aerospace Conference*, IEEE, 2018, pp. 1–18.

[23]Lin, J. K., Shook, L. S., Ware, J. S., and Welch, J. V., "Flexible material systems testing," *NASA Contractor Report*, 2010.

[24]Brehm, C., Barad, M. F., Housman, J. A., and Kiris, C. C., "A comparison of higher-order finite-difference shock capturing schemes," *Computers & Fluids*, Vol. 122, 2015, pp. 184–208.

[25]Wang, B., Xiang, G., and Hu, X. Y., "An incremental-stencil WENO reconstruction for simulation of compressible two-phase flows," *International Journal of Multiphase Flow*, Vol. 104, 2018, pp. 20–31.

[26]Mittal, R., Dong, H., Bozkurttas, M., Najjar, F., Vargas, A., and von Loebbecke, A., "A versatile sharp interface immersed boundary method for incompressible flows with complex boundaries," *Journal of Computational Physics*, Vol. 227, No. 10, 2008, pp. 4825–4852.

[27]Nakahashi, K., "Immersed boundary method for compressible Euler equations in the building-cube method," *20th aiaa computational fluid dynamics conference*, 2011, p. 3386.

[28]Berndt, R. J., "Supersonic Parachute Research," Tech. rep., AERONAUTICAL SYSTEMS DIV WRIGHT-PATTERSON AFB OH FLIGHT ACCESSORIES LAB, 1962.

[29]Cruz, J. R., O'Farrell, C., Hennings, E., and Runnells, P., "Permeability of Two Parachute Fabrics-Measurements, Modeling, and Application," *24th AIAA Aerodynamic Decelerator Systems Technology Conference*, 2017, p. 3725.

[30]Lee, Y., Lee, P.-S., and Bathe, K.-J., "The MITC3+ shell element and its performance," *Computers & Structures*, Vol. 138, 2014, pp. 12–23.

[31]Jeon, H.-M., Lee, Y., Lee, P.-S., and Bathe, K.-J., "The MITC3+ shell element in geometric nonlinear analysis," *Computers & Structures*, Vol. 146, 2015, pp. 91–104.

[32]Lee, P.-S. and Bathe, K.-J., "Development of MITC isotropic triangular shell finite elements," *Computers & Structures*, Vol. 82, No. 11, 2004, pp. 945–962.

[33]Dvorkin, E. N., Onte, E., and Oliver, J., "On a non-linear formulation for curved Timoshenko beam elements considering large displacement/rotation increments," *International Journal for Numerical Methods in Engineering*, Vol. 26, No. 7, 1988, pp. 1597–1613.

[34]Boustani, J., Barad, M. F., Kiris, C. C., and Brehm, C., "An immersed boundary fluid–structure interaction method for thin, highly compliant shell structures," *Journal of Computational Physics*, Vol. 438, 2021, pp. 110369.

[35]Boustani, J., Anugrah, G., Barad, M. F., Kiris, C. C., and Brehm, C., "A Numerical Investigation of Parachute Deployment in Supersonic Flow," *AIAA Scitech 2020 Forum*, 2020, p. 1050.

[36]Wald, I., Woop, S., Benthin, C., Johnson, G. S., and Ernst, M., "Embree: a kernel framework for efficient CPU ray tracing," *ACM Transactions on Graphics (TOG)*, Vol. 33, No. 4, 2014, pp. 1–8.

[37]Celik, I. B., Ghia, U., Roache, P. J., and Freitas, C. J., "Procedure for estimation and reporting of uncertainty due to discretization in CFD applications," *Journal of fluids Engineering-Transactions of the ASME*, Vol. 130, No. 7, 2008.